

Article

Unsteady Loading on a Tidal Turbine Due to the Turbulent Wake of an Upstream Turbine Interacting with a Seabed Ridge

Sulaiman Hurubi ^{1,2} , Hannah Mullings ¹ , Pablo Ouro ^{1,*} , Peter Stansby ¹  and Tim Stallard ¹ 

¹ School of Engineering, University of Manchester, Manchester M13 9PL, UK; sulaiman.hurubi@postgrad.manchester.ac.uk (S.H.); hannah.mullings@manchester.ac.uk (H.M.); p.k.stansby@manchester.ac.uk (P.S.); tim.stallard@manchester.ac.uk (T.S.)

² Department of Civil and Architectural Engineering, Jazan University, Jazan 45142, Saudi Arabia

* Correspondence: pablo.ouro@manchester.ac.uk

Abstract: Tidal sites can present uneven seabed bathymetry features that induce favourable or adverse pressure gradients and are sources of turbulence, and so are likely to affect the operation, performance, and wake recovery dynamics of deployed tidal-stream turbines. Large-eddy simulations are conducted to analyse the unsteady loading of a tidal turbine subjected to the wake of an upstream turbine that interacts with a two-dimensional ridge located between the two turbines. Relative to an isolated turbine, blade fatigue loading is increased by up to 43% when subject to the wake of a turbine located 8 turbine diameters upstream interacting with a ridge located 2 turbine diameters upstream, whereas for the same spacing, the turbine wake led to a limited 6% reduction in loading and the ridge wake only caused a 79% increase. For larger spacings, the trends were similar, but the magnitude of difference reduced. Predictions of fatigue loads with a blade element momentum model (BEMT) provided a good agreement for flat bed conditions. However, the ridge-induced pressure gradient drives rapid spatial change of coherent flow structures, which limits the applicability of Taylor's frozen turbulence hypothesis adopted in the BEMT. Reasonable prediction of rotor loading with BEMT was found to be obtained using the turbulent onset flow field at a plane one-diameter upstream of the turbine. This is more accurate than use of the planes at the rotor plane or two-diameters upstream, as coherent structures represent those modified by wake recovery and rotor induction in the approach flow to the turbine.

Keywords: tidal stream turbines; bathymetry; large-eddy simulation; wake recovery; tidal arrays; turbine fatigue loads



Academic Editor: Davide Astolfi

Received: 6 December 2024

Revised: 17 December 2024

Accepted: 18 December 2024

Published: 2 January 2025

Citation: Hurubi, S.; Mullings, H.; Ouro, P.; Stansby, P.; Stallard, T. Unsteady Loading on a Tidal Turbine Due to the Turbulent Wake of an Upstream Turbine Interacting with a Seabed Ridge. *Energies* **2025**, *18*, 151. <https://doi.org/10.3390/en18010151>

Copyright: © 2025 by the authors. Licensee MDPI, Basel, Switzerland. This article is an open access article distributed under the terms and conditions of the Creative Commons Attribution (CC BY) license (<https://creativecommons.org/licenses/by/4.0/>).

1. Introduction

Tidal-stream energy harnesses kinetic energy from the predictable movement of ocean tides, with a great potential as a renewable energy source in countries such as the United Kingdom, France, Canada, Japan, Australia, the Philippines, and China, among others [1–7]. At tidal-stream project sites, tidal turbine arrays consist of multiple devices that need to be strategically positioned to capture strong tidal flows whilst minimising the impact of wake effects on power performance and fatigue loading of interacting turbines [8,9]. The expansion of tidal arrays in a relatively narrow set of locations worldwide demands the careful micro-siting of turbines that accounts for local bathymetric features and effects from other turbines to ensure the array operates in an efficient and cost-effective manner [10,11]. To ensure this is achieved, capturing the wake evolution, especially its recovery rate, is crucial to optimise the performance and operating life of tidal energy arrays.

In tidal environments, the effects of bathymetry can be considered in terms of two features; roughness (height variation over relatively small spatial scales) and slope (height variation over larger spatial scales causing a change to the mean flow speed). Changes in the seabed elevation, i.e., slope, can lead to pressure gradients that accelerate or decelerate the flow velocity, depending on the slope or height of bathymetry features. Different studies in tidal arrays and wind farms have shown that when a turbine's wake encounters a favourable pressure gradient (FPG), it positively impacts the recovery rate of the turbine's wake [12–17]. For instance, Shamsoddin & Porté-Agel [18] investigated numerically the impact of a two-dimensional hill on the wake of a wind turbine located upstream of it, observing that the wake recovery along the wake's centreline was enhanced. In the context of tidal turbines, the large-eddy simulation (LES) results from Hurubi et al. [19] demonstrated that when turbines operate upstream of a ridge, the downstream rate of recovery of the disc-averaged velocity along the wake centre increases compared to flat-bed conditions. More recently, Hurubi et al. [20] studied the effect of a two-dimensional ridge on turbine siting. Their results showed that when a ridge is located in the turbine's wake, the wake passes through the ridge's favourable and adverse pressure sides, corresponding to its upstream and downstream halves, respectively. Although adverse pressure gradient (APG) is known to result in a longer wake recovery distance, its effect varied depending on the relative distance of the turbine to the ridge; specifically, a turbine-to-ridge-centre distance greater than $1.5D$ promoted a faster wake recovery, implying the FPG effect dominated over the APG in the turbine wake recovery. An FPG contributes to a quicker recovery rate in the turbine wake, which is advantageous for the energy available at the secondary rows of turbines. An enhanced wake recovery rate increases the onset flow velocity at downstream turbines, thereby increasing their available kinetic energy. In the numerical study of a six-turbine tidal array by Ouro et al. [9], the bathymetry at the deployment location (Shetland Isles, UK) featured a slope of about 10° between the two rows. During flood tide, FPG conditions were developed as the flow moved from deeper water at the first-row locations to a shallower region at the second row, spaced $12D$ downstream. The wake of the first-row turbines recovered more rapidly compared to the ebb tide, in which an APG was developed. Hyvärinen & Segalini [21] investigated the flow around two aligned wind turbines situated on a series of sinusoidal hills. They observed an increase in power performance in the downstream turbines compared to flat-terrain scenarios. In a similar turbine arrangement, Sigüenza-Alvarado et al. [16] carried out experiments on a two-dimensional hill with varying slopes, showing that the FPG positively influenced wake recovery, especially on steep hills. Dar & Porté-Agel [22] conducted wind tunnel experiments with two aligned wind turbines on linear ramps to investigate induced pressure effects. They demonstrated that the velocity deficit behind the first row reduces in FPG cases, especially when increasing the ramp slope, in contrast to flat-bed and APG scenarios.

Bathymetry-induced turbulence and flow coherent structures also play an important role in wake recovery mechanisms and may lead to a shorter lifespan for downstream turbines due to an increase in fatigue loading [20,23–25]. Ouro et al. [26] highlighted that compared to a flat-bed scenario with lower turbulence, turbulence induced by bathymetry positively influences the wake recovery rate by enhancing the turbulent transport of momentum. In terms of ultimate and fatigue loads, consideration needs to be taken for extreme flow conditions such as high turbulence intensity, high flow velocity, and highly sheared flow [23,24,27]. Hurubi et al. [20] showed that the complex flow generated by a turbine wake interacting with a seabed ridge can cause the fatigue loads on the turbine's blades to reach a peak that is 70% higher than those observed in a flat-bed scenario. When operating in a tidal array with a fully aligned layout, the reduction in the onset flow velocity

due to wakes of upstream turbines contributes to lowering their fatigue loads despite the increase in turbulence intensity [28].

Building upon previous research by the authors Hurubi et al. [20], this study uses LES to assess the wake dynamics on two fully aligned tidal-stream turbines and specifically examines the loading on the downstream turbine, both operating in proximity to a seabed ridge and compared to a flat-bed scenario. In particular, turbines positioned $2D$ and $6D$ upstream of the ridge centre are considered due to the improved wake recovery rate shown in previous a study by the authors [20]. When turbines are downstream of the ridge, the fatigue loads increase due to ridge-induced shear and heterogeneous turbulence distribution over the rotor's swept area. The objective of this research is threefold: first, to assess whether the beneficial pressure gradient induced by the ridge can offset the increased fatigue loads on turbines positioned downstream of the ridge; second, to investigate whether the downstream turbine wakes feature an axisymmetric wake shape, and whether its induction region can be captured following vortex-sheet theory; and third, to evaluate the effectiveness of blade element momentum theory in predicting loading on downstream turbines under varying onset conditions.

2. Numerical Methods

The loading caused by the turbulent wakes of both a ridge and an upstream turbine on a downstream device is mainly assessed using high-fidelity LES. Specifically, the in-house Digital Offshore Farm Simulator (DOFAS) [28] code is used, which has been previously validated to investigate wake recovery processes and quantify the structural loads on single, and arrays of, tidal stream turbines [9,19,28,29]. From the LES, the computed forces are compared with predictions derived from the in-house Blade Element Momentum Theory (BEMT) code Maya [30,31], which employs time-varying onset flow planes extracted from LES precursor simulations [32].

2.1. DOFAS: In-House LES Solver

DOFAS utilises a staggered-storage approach to store velocities and pressure on rectangular Cartesian grids, and is parallelised with the Message Passing Interface (MPI) protocol, achieving excellent computational efficiency and scalability [33]. DOFAS solves the spatially-filtered Navier–Stokes equations for unsteady and incompressible viscous flows,

$$\frac{\partial u_i}{\partial x_i} = 0 \quad (1)$$

$$\frac{\partial u_i}{\partial t} + \frac{\partial(u_i u_j)}{\partial x_j} = -\frac{1}{\rho} \frac{\partial p}{\partial x_i} + \nu \frac{\partial^2 u_i}{\partial x_j \partial x_j} - \frac{\partial \tau_{ij}}{\partial x_j} + f_i, \quad (2)$$

where u_i is the resolved velocity component in the $i = 1, 2$, or 3 , denoting the special coordinates in the x -, y -, and z -axis directions, respectively, ρ is the density of the fluid, p is the resolved pressure, and ν is the kinematic viscosity of the fluid. The convection and diffusion terms in the momentum equation are discretised using a second-order central difference scheme and a low storage two-step Runge–Kutta method is employed for time advancement. To correct predicted velocities, a Poisson pressure equation is solved using a multi-grid technique within an explicit fractional step method [34]. The subgrid scale stress tensor is approximated using the wall-adapting local-eddy viscosity (WALE) model [35]. The source term f_i accounts for the external forces from the moving turbine's rotor blades and solid bodies such as the turbine's support structures and ridge.

For the turbine rotor representation, DOFAS adopts an Actuator Line Method (ALM) [36]. The ALM divides each blade into multiple dynamic Lagrangian markers, distributed along its length based on the adopted grid resolution. The present ALM em-

employs a non-isotropic Gaussian projection [37] for the interpolation process, together with a Prandtl-type tip-loss correction [38]. For the representation of the seabed ridge and turbine's vertical support structure, a direct-forcing Immersed Boundary Method (IBM) [39] is used. DOFAS has been widely tested and used for single tidal stream turbines operating in complex conditions such as waves [29] and bathymetry [19,20,26] and in tidal arrays [9,28].

2.2. The BEMT Model

Maya is an in-house unsteady BEMT code, based in MATLAB v2024a, that has been validated against experimental data [31], and widely applied using synthetic onset turbulent flow fields [27,30], as well as the flow field from LES [32]. Within the code, axial and tangential induction to the rotor are calculated, with tip and hub losses accounted for through Prandtl's tip loss and Glauert's correction for highly loaded rotors where needed. For time-varying unsteady onset flow, the code determines the relative velocity at multiple positions along the blade (blade elements), and the inflow angle based upon the rotational position of the blade at each time step of the turbulent flow field. These conditions are then used to determine the tangential and normal loads along the blades, with a view to establishing performance and loading characteristics for the turbine. This method has been shown to provide efficient predictions of the loading similar to that of the LES-ALM when the same inflow is used, and can be utilised to provide load predictions within an array at a lower computational cost than setting up a large CFD model [32].

2.3. Description of Test Cases and the Computational Setup

Building upon previous research by Hurubi et al. [20], this study employs the same simulation framework using the laboratory-scale tidal-stream turbine from Stallard et al. [40]. Figure 1 presents the computational domain measuring $49D$ long, $15.5D$ wide, and $2D$ deep, with D being the turbine's rotor diameter, including the position of the ridge and relative location of the two fully-aligned tidal turbine configurations. The geometry of the ridge is modelled with a Gaussian shape described as:

$$Z_h(x) = \frac{1}{2}h \left[1 + \cos\left(\frac{\pi x}{l}\right) \right], \quad (3)$$

here, $h = 0.33D$ represents the height of the ridge, and $l = D$ denotes the length of one side of the Gaussian ridge's base, making the total length of the ridge equal to $2D$. The turbine has a diameter (D) of 0.27 m, a hub height of 0.225 m, and is mounted on a bottom-fixed vertical support structure with a diameter of 0.015 m. To ensure consistency and comparability across different scenarios, the total open-channel depth is kept constant, being in cases when the ridge is modelled at a total water depth of $H = 0.54$ m. The ridge height is $0.33D$ such that the minimum water depth is 0.45 m ($1.67D$). The mean velocity is $U_0 = 0.47$ m/s. A uniform, isotropic cell size of $\Delta_i = 0.0185D$ is used in all spatial directions, equivalent to 54 grid points across the rotor diameter, which achieves a total number of approximately 285 million cells. A fixed time step (Δt) of 0.001 s is adopted, and the simulations run for 260 s of physical time. First-order statistics are collected after the initial 30 s to discard initial flow transients, and second-order statistics are gathered after an additional 30 s.

The inflow profile used at the inlet replicates the vertical shear profile and turbulence statistics measured in the experiment [40]. The instantaneous inflow velocities are computed as

$$\frac{u(y, z)}{u^*} = \frac{1}{\kappa} \ln\left(\frac{u^* z}{\nu}\right) + C + u'_{SEM}(y, z), \quad (4)$$

where $u^* = 0.0187$ m/s is the friction velocity, $\kappa = 0.41$ is the von-Kármán constant, $C = 5$ is the smooth channel constant, and u'_{SEM} is the turbulent velocity fluctuation imposed using the Synthetic Eddy Method (SEM) [41], which adopts a turbulence intensity (TI) of 15% and length scales of $L_x = 0.56H$, $L_y = 0.33H$, and $L_z = 0.25H$ in the x -, y -, and z -directions, respectively.

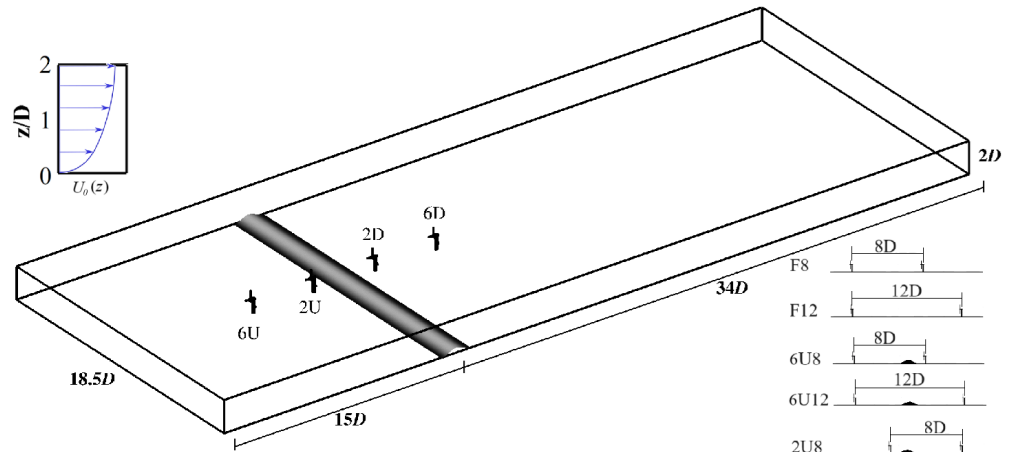


Figure 1. Representation of the computational domain includes a seabed ridge with dimensions expressed in turbine diameters D . The two-turbine configurations studied in the presence of a ridge are 6U8, 6U12, and 2U8. The same spacings between turbines are also tested for flat-bed conditions, labelled as F8 and F12.

At the outlet, a convective outflow boundary condition is set in the LES, a free-slip condition is applied at the top surface, and periodic boundary conditions are adopted in the spanwise boundaries.

To analyse the loads on the second-row turbines, two different spacings between turbines are considered, namely, $8D$ and $12D$. These layouts are examined both with and without a ridge present, and illustrated in Figure 1. The nomenclature used to describe the different layouts that include two turbines is:

- Flat-bed cases (no ridge): “ FN ”, with “ N ” denoting the row spacing in terms of turbine diameters,
- Single turbine: “ ND ” or “ NU ”, with “ N ” being the ridge-turbine distance in terms of turbine diameters and “ D ” and “ U ” denoting the relative position to the ridge,
- Two turbines: “ NUM ”, with “ N ” being the distance of the first turbine to the ridge centre and “ M ” the spacing between the two turbines, both in terms of turbine diameters.

During operation, the turbine achieved an optimal tip speed ratio ($TSR = D\Omega/2U_0$) of 4.43, with thrust and power coefficients of $C_x = 0.82$ and $C_p = 0.30$ [40], which was adjusted for all turbines using the disc-averaged velocity at the rotor plane obtained from precursor simulations. These precursor simulations were run without the turbine of interest to collect onset flow data, which was then used to adjust the turbine’s rotational speed and as input to the BEMT code (Section 2.2). The disc-averaged velocity, U_D , is calculated as follows:

$$U_D = \frac{1}{A_D} \sum U(x, y, z) dA \quad (5)$$

where $U(x, y, z)$ represents the mean streamwise velocity at any point within the turbine’s rotor disc area A_D . Table 1 presents the inflow conditions in terms of normalised disc-averaged mean velocity (U_D/U_0) and turbulence intensity (u'_D/U_0) at each turbine position

considered, and its rotational speed according to its optimal TSR. The velocity deficit is computed as follows:

$$\Delta U(x, y, z) = U_b(x, y, z) - U_t(x, y, z). \quad (6)$$

where U_b and U_t represent the mean velocity fields of the base-flow simulation and that including the turbine of interest, respectively.

Table 1. Comparison of normalised disc-averaged mean velocity (U_D/U_0) and turbulence intensity (u'_D/U_0) at turbine positions for the flat-bed case (TF), with the first-row turbine positioned 6 diameters (6U) or 2 diameters (2U) upstream of the ridge and with the second-row turbine only. The rotational speed (Ω) is specified based on U_D to maintain a consistent tip speed ratio of 4.43 at all turbine positions.

Configuration	U_D/U_0 -	u'_D/U_0 %	Ω rad/s
Flat bed			
TF	1.01	7.60	15.66
F8	0.80	11.83	12.30
F12	0.86	10.34	13.28
First-row 6D upstream of the ridge			
6U	1.02	7.68	15.66
6U8	0.99	13.24	15.30
6U12	0.92	12.59	14.17
First-row 2D upstream of the ridge			
2U	1.02	7.44	15.71
2U8	0.83	13.52	12.85
Second-row only (no upstream turbine)			
2D	1.16	12.76	17.82
6D	1.03	9.97	15.84

2.4. Fatigue Loads Calculations

Following the approach of [20,31,42], Damage Equivalent Loads (DEL) are utilised to assess the fatigue loading on the turbine blades depending on the onset flow conditions, which can be calculated based on LES and BEMT data. The DEL values are calculated based on:

$$\text{DEL} = \left(\frac{\sum_i n_i F_i^m}{N} \right)^{\frac{1}{m}}. \quad (7)$$

In the present analysis, a Rainflow counting method is employed to identify the load cycles (n_i) and classify their corresponding load ranges (F_i) [43]. This method has been widely used in wind and tidal turbine studies [23,32,42,44,45]. The method involves sorting the identified load cycles into bins based on their load range, which enables the determination of the cycle counts for each load range bin (i), calculated over the considered turbine revolutions, represented by N , to correspond to the total number of revolutions over the entire simulation period. The blade is assumed to be made of a composite material characterised by an S–N curve with a slope of $m = 10$ [30,31].

3. Results

In this section, the mean flow velocity is first characterised through analysis of horizontal and vertical planes through the turbine axis, followed by an analysis of the velocity

deficit in the wake region of the downstream turbines. Subsequently, the evolution of disc-averaged velocity and turbulence intensity in the streamwise direction are quantified. Finally, the blade loads from the LES-ALM are studied and compared to predictions from the BEMT with LES-generated onset flow data.

3.1. Flow Field

The distribution of mean streamwise velocity for the flat-bed cases with a single turbine (TF) and with two turbines spaced at $8D$ (F8) and $12D$ (F12) is presented in Figure 2 as horizontal and vertical contour planes across the turbine's centre. The velocity contours show the spatial evolution of the wake of the first-row turbine (case TF in Figure 2), with the low-velocity wake region observed at distances of $8D$ and $12D$ where the second turbine is deployed, and hence turbine-wake interactions occur. This is quantified in Table 1 with the disc-averaged velocity for the second turbine, being 7.5% larger at F12 than F8. In terms of turbulence in the flat-bed scenarios, Table 1 shows that the disc-averaged turbulence intensity is 55.7% and 36.1% greater at the F8 and F12 locations, respectively, compared to the single-turbine case (TF).

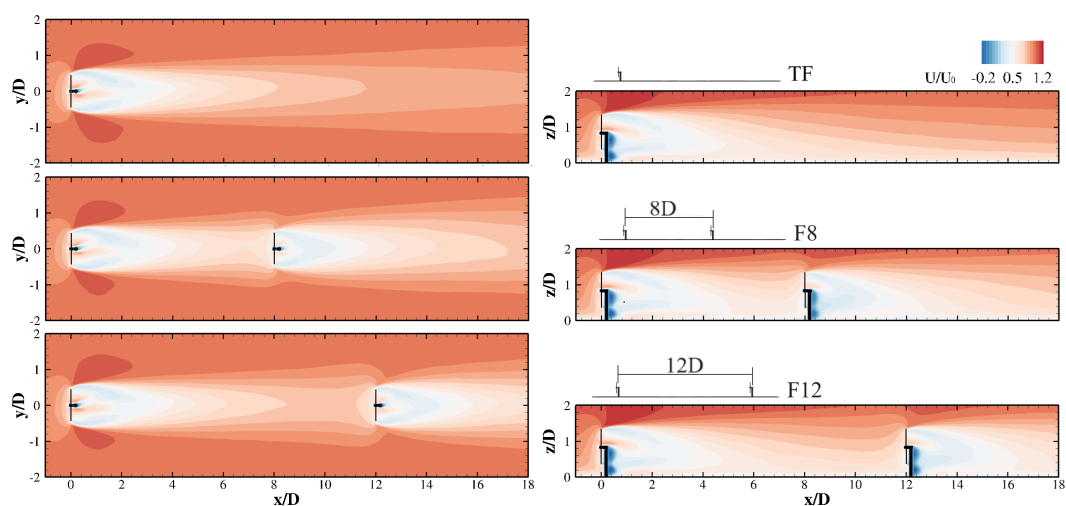


Figure 2. Mean streamwise velocity (U/U_0) distribution of the cases with a flat-bed (TF for a single turbine and F8 and F12 for two turbines). Horizontal (left) and vertical (right) contours across the turbine centre are shown with the origin of coordinates at the first-row turbine.

For configurations with the ridge, Figure 3 presents horizontal and vertical contours of mean streamwise velocity across the turbine's centre. With the first-row turbine positioned $6D$ upstream of the ridge (6U), two spacings with the downstream turbine are simulated, namely, $8D$ (6U8) and $12D$ (6U12). While the turbines in the 6U12 configuration are symmetrically located around the ridge, the reverse flow heading to occur during a tidal phase is considered for 6U8 by adding the case 2U8, in which the upstream turbine operates $2D$ upstream of the ridge. There is a positive impact of the ridge-induced FPG on the wake recovery of the first-row turbine for cases 6U and 2U (Figure 3) compared to flat-bed conditions (TF in Figure 2). Compared to F8, the ridge causes an increase in the disc-averaged velocity of the second turbine by 23.75% for case 6U8 and 3.75% for 2U8 (Table 1). Similar occurs for the larger streamwise spacing; the disc-averaged velocity at the second-row turbine location in the 6U12 case is 7% greater than for the F12 configuration. This increase in onset velocity suggests that the ridge helps to reduce the impact between the two turbines. Moreover, the increase in recovery rate compared to the flat-bed configuration in the 2U8 case is not as significant as in the 6U8 case that has the same turbine spacing, reflecting that when the upstream turbine is further away from the ridge, the effect of the FPG has a greater impact on the wake recovery rate than the APG.

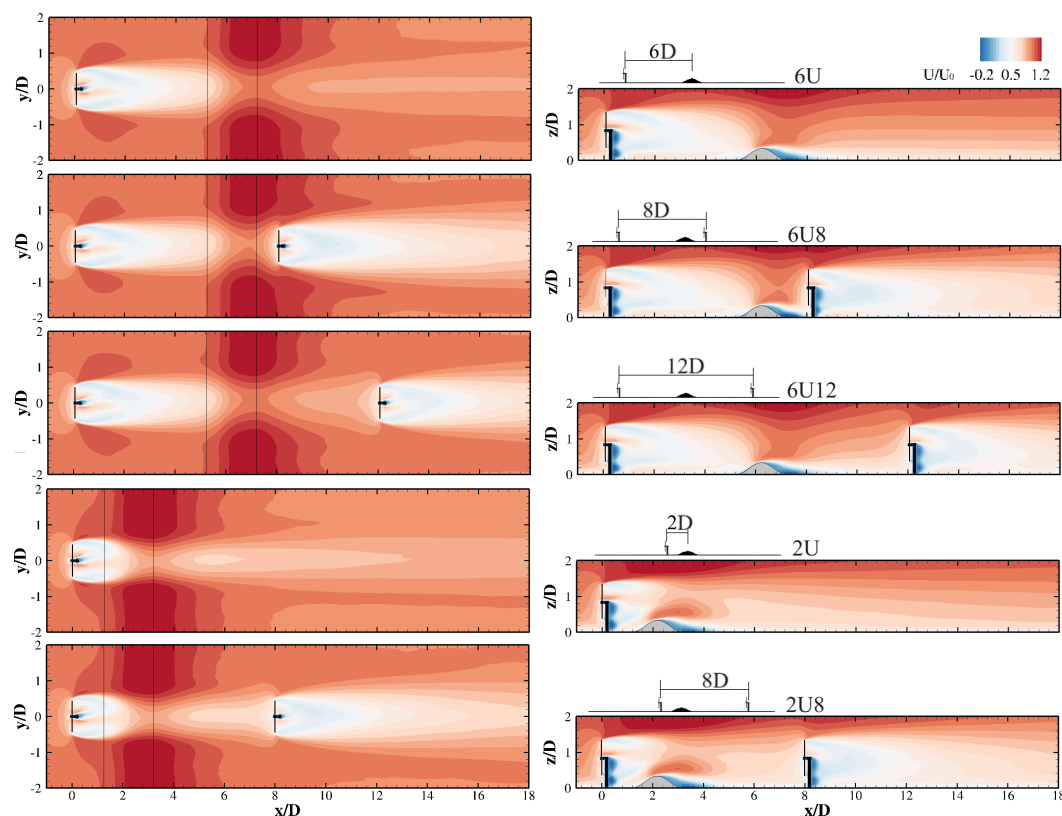


Figure 3. Mean streamwise velocity (U/U_0) distribution of the ridge cases (6U and 2U for a single turbine and 6U8, 6U12 and 2U8 for two turbines). Horizontal (**left**) and vertical (**right**) contours across the turbine centre are shown with the origin of coordinates at the first-row turbine.

For layouts where the first-row turbine is $6D$ upstream of the ridge (6U), the disc-averaged turbulence intensity (u'_D) at the second-row turbine locations, 6U8 and 6U12, increases by about 12% and 22%, respectively, compared to their counterparts in the flat-bed scenario, i.e., F8 and F12 (Table 1). A 14.3% increase in u'_D is observed at the downstream turbine in the 2U8 case compared to the flat-bed with the same turbine spacing (F8). In all ridge cases, the increase in u'_D at the second turbine is mainly due to the upstream turbine's wake rather than the ridge, observed when comparing values for the second turbine without the upstream device (Table 1). Specifically, the case 6U8 has about 4% more turbulence than the 2D case, and in the case 6D u'_D is reduced by 26% and 35.6% compared to cases 6U12 and 2U8, and is also lower than in flat-bed scenarios (cases F8 and F12). This suggests that the contribution from the turbulence of the first-row turbine's wake in the presence of the ridge is less significant compared to the flat-bed cases.

The streamwise velocity deficit contours for simulations with the first-row turbines only and with the two-turbine cases for both flat-bed and ridge configurations are presented in Figures 4 and 5, respectively. Note that by applying Equation (6) to the cases with two turbines, the deficit of the downstream turbines here shows the evolution of its wake after removing the influence of the wakes from both the ridge and upstream turbine. This separates the impact of the upstream flow conditions on the downstream turbine and its wake. It is worth noting that turbines are always set to operate at a constant tip speed ratio, ensuring a constant ratio of momentum extraction (Table 1).

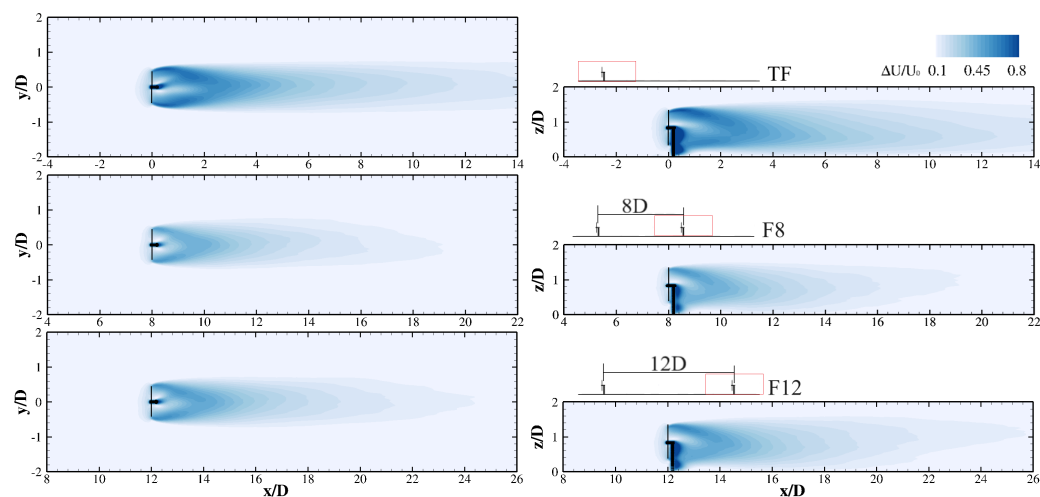


Figure 4. Horizontal (left) and vertical (right) contours of normalised velocity deficit ($\Delta U/U_0$) across turbine's centre in the flat-bed configurations (TF for a single turbine and F8 and F12 for two turbines). The deficit in cases with two turbines is computed by subtracting the mean velocity field from the two-turbine simulation from that with the first-row turbine only. The streamwise origin of coordinates is taken at the first-row turbine rotor location.

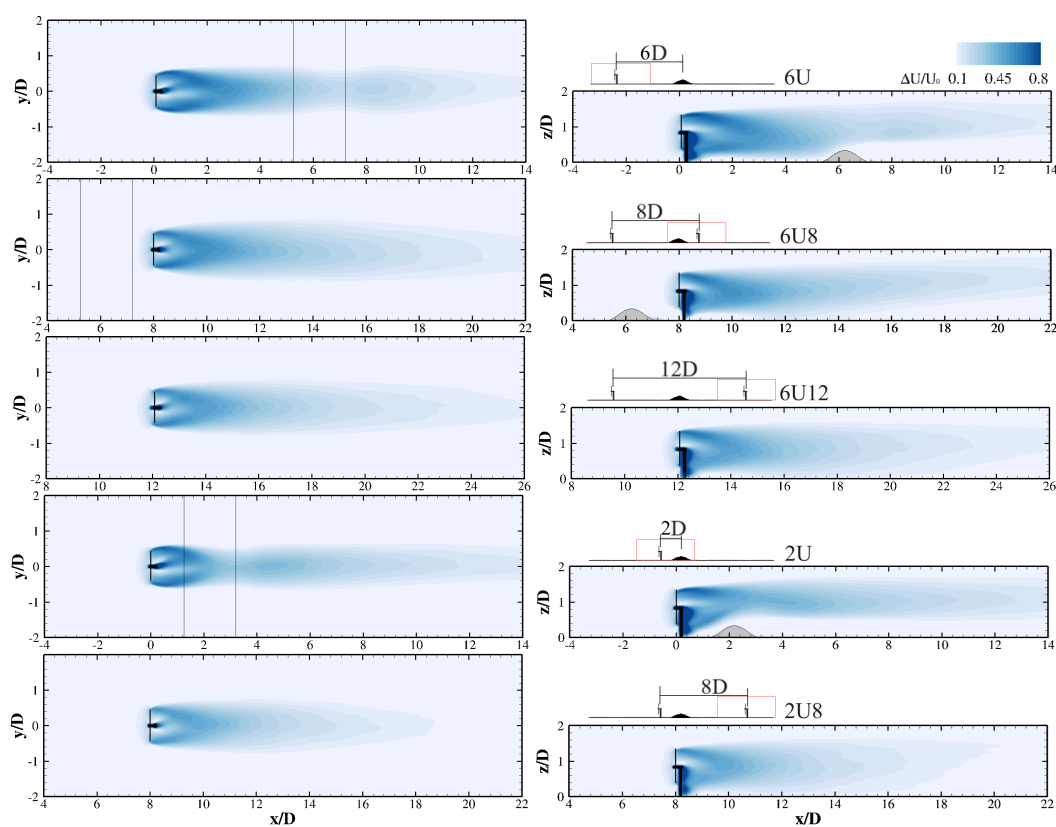


Figure 5. Horizontal (left) and vertical (right) contours of normalised velocity deficit ($\Delta U/U_0$) across turbine's centre in the ridge configurations (6U and 2U for a single turbine and 6U8, 6U12, and 2U8 for two turbines). The deficit in cases with two turbines is computed by subtracting the mean velocity field from the two-turbine simulation from that with the first-row turbine only. The streamwise origin of coordinates is taken at the first-row turbine rotor location.

The velocity deficit downstream of the second-row turbines in the flat-bed configurations F8 and F12 decreases compared to the TF case (Figure 4). For cases when the ridge is present, the velocity deficit downstream of the second-row turbine in the 6U8 and 6U12

cases (Figure 5) has a similar spatial distribution to the TF case (Figure 4). In these cases, at the downstream turbine position, the wake of the first-row turbine is mostly recovered due to the pressure gradients of the ridge, thus having limited effect on the velocity deficit field around the second-row turbine. This improved recovery is evident in the wake of the 6U case downstream of the ridge (Figure 5) and in U_D for the 6U8 and 6U12 cases (Table 1). In addition to the effect from the wake of first-row turbine, the wake of the second-row turbine in the 6U8 case is also affected by the ridge-induced APG, which slows the wake recovery rate further downstream.

The wake downstream of the modelled turbine in isolation was shown to follow a semi-empirical Gaussian wake model for flat-bed scenarios, where the wake was characterised as self-similar and two-dimensional beyond $x/D \geq 8$ [40]. This is now re-assessed for the second-row turbines. The self-similar nature of the wake of the second-row turbines is analysed with transverse profiles of velocity deficit downstream of the flat-bed case and the second-row turbines at streamwise distances (x/D) from 2 to 20 (Figure 6), and normalised by the maximum velocity deficit ΔU_{max} and wake half-width $y_{1/2}$ at each location. The profiles of the wake deficit show that the transverse expansion of the second-row turbine wakes follows the Gaussian wake model (dashed line in Figure 6) up to $y/y_{1/2} < \pm 1$ with reduced velocity deficit at $y/y_{1/2} \geq \pm 1$ at all downstream locations. The wake expansion is impacted by the onset flow conditions, with the 6U8 case having the lowest velocity deficit (negative deficit) due to the flow acceleration around the wake region. Deviation from the Gaussian wake model increases at $x/D = 20$, but overall, the wake profile is in reasonable agreement with the Gaussian model for all locations. Furthermore, it is only in the absence of the effect of an upstream turbine, i.e., in the TF case only, that LES underestimates the maximum deficit at $x/D \leq 2$, where the wake is axisymmetric [28,40].

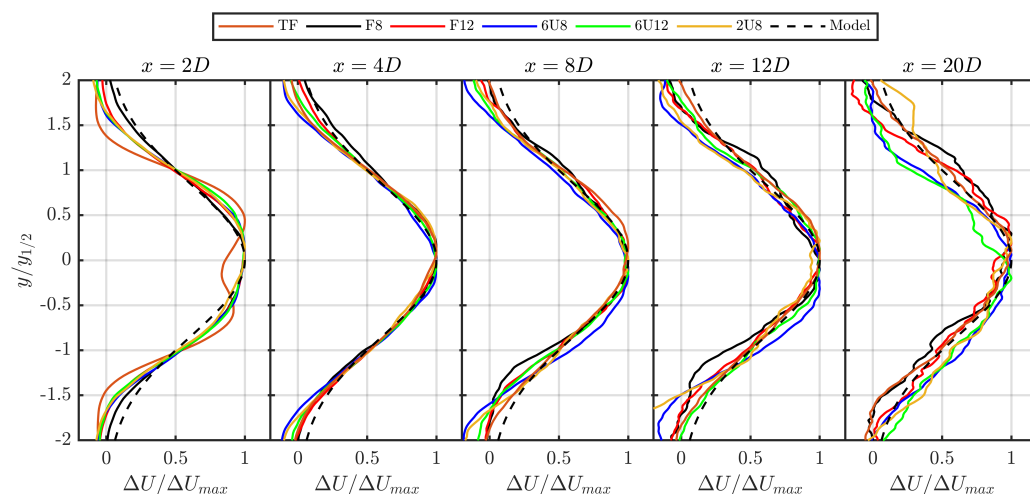


Figure 6. Transverse profiles of the velocity deficit at hub height for the flat-bed cases (TF, F8, and F12) and two-turbine configurations (6U8, 6U12, and 2U8) compared with the theoretical Gaussian shape model. The data are normalised by the maximum velocity deficit, ΔU_{max} , and wake half-width, $y_{1/2}$.

The disc-averaged velocity and turbulence intensity for the second-row turbine locations for configurations with and without its operation are shown in Figure 7, including velocities upstream up to $x/D = -5$ and downstream until $x/D = 25$.

In terms of wake recovery, the ridge-induced APG decelerates the flow immediately downstream of the ridge, leading to slower recovery rates when the second-row turbine is in this region, as in the 6U8 case. For the latter, the disc-averaged velocity is consistently lower than in the 2U8 and 6U12 cases while featuring larger turbulence intensity over the wake region (Figure 7a). When the second-row turbine is positioned further downstream of the ridge, in cases 6U12 and 2U8, the recovery pattern is similar to the flat-bed layouts,

F8 and F12. These results suggest that the presence of the ridge between the two devices improves the wake recovery of the upstream turbine and enhances the wake recovery of second-row turbines positioned downstream. There are large variations in disc-averaged turbulence intensity when the turbulent wake from the first-row turbines merges with the ridge-induced turbulence; as seen in cases 6U8, 6U12, and 2U8 upstream of the second-row turbine, $x/D \leq 0$, compared to the F8 and F12 cases (Figure 7b). The ridge induces oscillation in turbulence intensity, rather than the purely monotonic decay observed in the flat-bed case. This can also be observed in the shear stress for the same configuration (see Figure 8 in [20]).

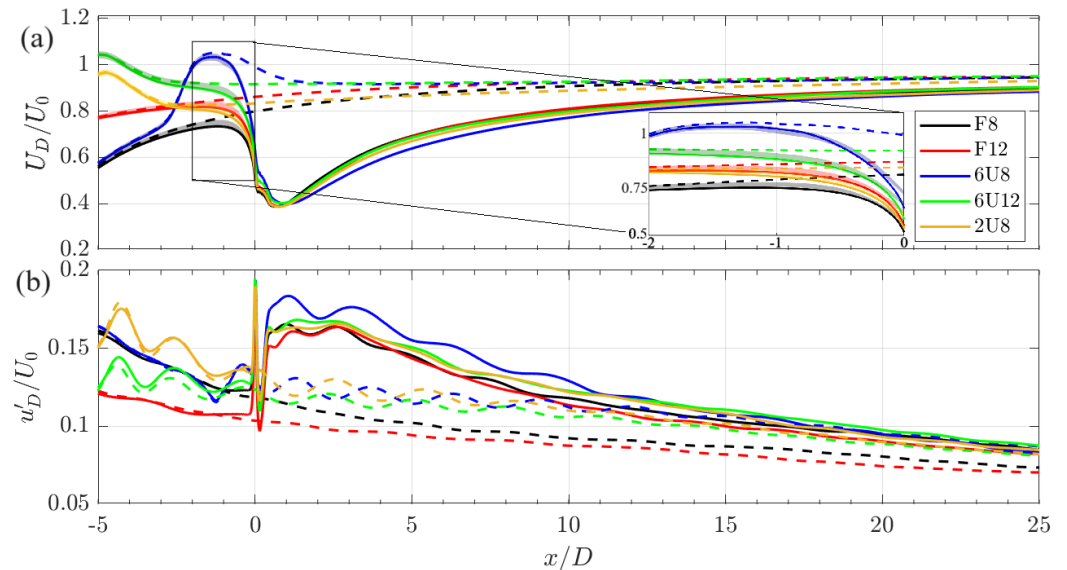


Figure 7. Streamwise evolution of the normalised disc-averaged (a) velocity (U_D/U_0) and (b) turbulence intensity (u'_D/U_0) computed at hub height. Data from configurations with the first-row turbines only (dashed lines) and with second-row turbines (solid lines) are compared. Here, $x/D = 0$ corresponds to the rotor location of the second-row turbines. Shaded area and detail (in a) upstream of the second-row turbine represents $\pm 1.5\%$ range of the predicted induction velocities based on applying vortex sheet theory (Equations (8) and (9)) to the base-flow.

The second turbine generates an upstream induction region affecting its disc-averaged streamwise velocity and turbulence intensity. This affects the flow up to $x/D = -5$ for case 6U12, but the extent varies depending on the configuration (Figure 7). For instance, a 10% difference in u'_D/U_0 at $x/D = -3$ is observed in case 6U12 compared to when no second-row turbine is present (6U), while less than 1.25% difference is found in the other cases. Despite the complexity of the spatially varying flows simulated, a good estimate of the velocity reduction in the induction region can be obtained from the base-flow simulation, i.e., with the upstream turbine, and the ridge when included, using vortex sheet theory [46]. The normalised disc-averaged onset flow is calculated as a function of the axial induction factor (a) and the turbine's mean thrust coefficient (C_x equal to 0.82), as:

$$a = \frac{1}{2} \left(1 - \sqrt{1 - C_x} \right) \quad (8)$$

$$\frac{U_D}{U_0} = 1 - a \left(1 + \frac{2x}{D} \left(1 + \left(\frac{2x}{D} \right)^2 \right)^{-\frac{1}{2}} \right). \quad (9)$$

A $\pm 1.5\%$ range of the predicted disc-averaged induction velocity is shown as shaded bands in Figure 7a. This approach has been successfully applied to predict onset velocities

in full-scale [47] and experimental [46,48] turbine studies, but not previously demonstrated for in-wake operation.

Whilst flow velocity reduces in the induction region, the presence of the second row turbine increases turbulence intensity relative to the base-flow of the upstream turbine wake only. The contribution of the wake and ridge, and both interacting wakes, can be observed in Figure 8. In particular, the impact of the upstream turbine wake on the ridge wake is observed in case 6U8, and to a lesser extent in 6U12. The turbulence distribution in the 2D and 6D cases is characterised by the presence of high turbulence near the bottom surface, as a result of the shear layer induced by the ridge wake (seen in the turbulent momentum flux, $-u'w'/U_0^2$, contours, Figure A1). These variations in onset velocity influenced by the upstream turbine and ridge can be expected to cause an increase in periodic loading as the blades rotate through regions with different velocities and turbulence properties. The presence of an upstream turbine reduces the turbulence intensity associated with the ridge wake around the bottom tip location of rotor blades when compared to ridge-only simulations, i.e., comparing 2D and 6U8 cases or 6D and 6U12 setups (Figures 8 and A1). While the turbulence across the rotor is more evenly distributed in the presence of a first-row turbine, the disc-averaged turbulence intensities remain higher compared to configurations with the ridge wake only (Table 1).

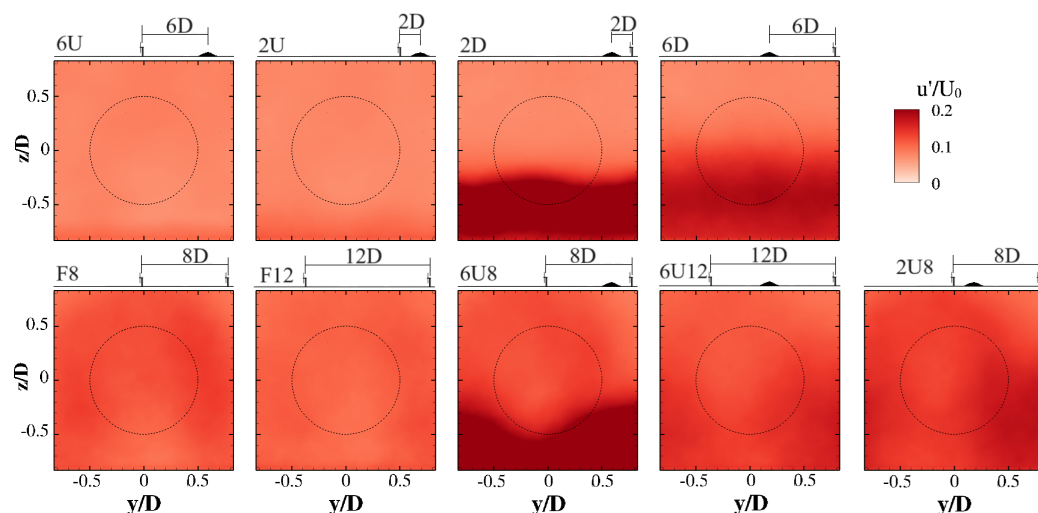


Figure 8. Turbulence intensity contours in the yz -plane from the base-flow simulations at the turbine locations of interest, with those in the top row being for configurations without upstream turbines and bottom row for scenarios where the upstream turbine is included. Dashed circles indicate the rotor swept area.

It is important to evaluate the heterogeneity of flow properties (velocity shear and turbulence) over the rotor plane to determine the impact on rotor loading. The variation in streamwise velocity and turbulence intensity across the rotor swept area (mostly vertically), together with the disc-averaged values, is shown in Figure 9. Note that only the TF case from the first-row turbine cases is shown in Figure 9, as similar onset flows are observed for all upstream turbine cases. Turbines operating downstream of the ridge only, 2D and 6D, experience a highly sheared inflow velocity along with heterogeneity in the turbulence intensity distribution (Figures 8 and 9b). For example, in the 6D case, the minimum mean streamwise velocity value is about 64.7% lower than U_D , while the maximum is only 8.6% larger than U_D . The reduced variations of mean streamwise velocity, compared to the disc-averaged values observed in the second-row turbines, suggests that the presence of a first-row turbine helps to minimise both the shear induced by the ridge and the heterogeneity in turbulence distribution across the rotor (Figure 9). Although the

second-row turbine in case 6U8 exhibits the highest mean velocity, indicating that more kinetic energy can be extracted at this location than any other two-turbine setup, it also experiences the largest variations in both velocity and turbulence (Figure 9). Furthermore, considering the bidirectional nature of tidal flows, the downstream turbine in case 6U12 leads to less variation in conditions than the combination of 6U8 and 2U8. In the former case, the incoming velocity is greater than that at the same location over flat-bed conditions (F12), while the shear and turbulence variation are lower compared to 6U8 and its reverse case 2U8.

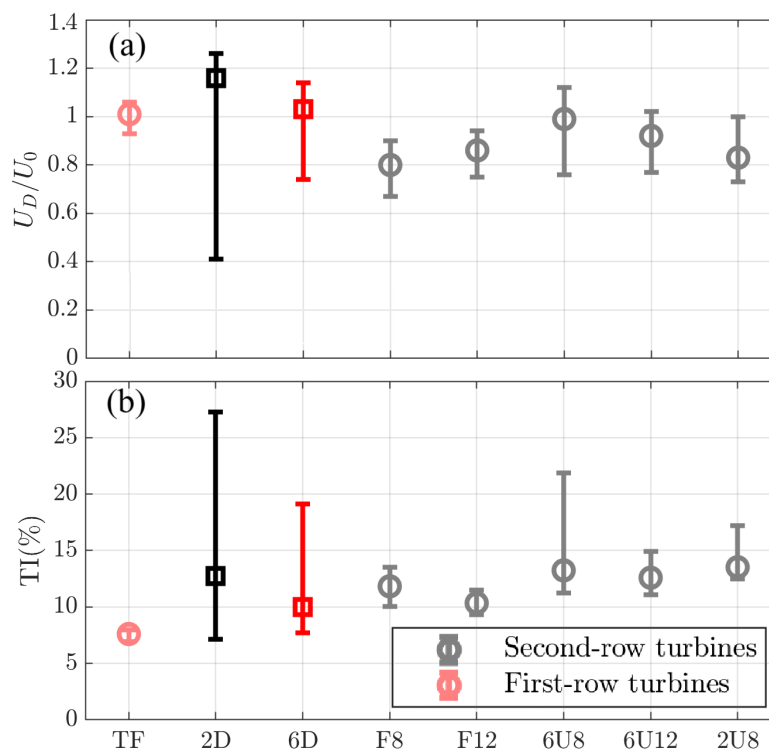


Figure 9. Comparison of the disc-averaged values (markers) of (a) streamwise velocity and (b) turbulence intensity at turbine positions from the base-flow with their maximum and minimum values over the swept area. Square markers are used for cases 2D and 6D to highlight the absence of first-row turbines while circular markers are adopted for the other cases.

3.2. Extreme and Fatigue Loading

In this section, the equivalent fatigue loads based on the thrust load on a single rotor blade are computed in terms of Damage Equivalent Load (DEL, defined in Equation (7)) from the time series of ALM forces over a duration of 200 s at a sampling frequency of 1000 Hz, corresponding to the inverse of the fixed time step adopted. The DEL values for all first-row turbines are all similar, being approximately $DEL_0 = 0.980$ N, as there are no changes in the upstream flow that affect these turbines. The flat-bed first-row turbine DEL_0 value is used to normalise the DEL obtained from second-row turbines (Table 2). Compared to scenarios where only the ridge is present upstream of the turbine, in the 2D and 6D cases, the fatigue load on the downstream turbine positions is the higher due to the larger shear and turbulence intensity being concentrated over the bottom tip of the rotor (Figure 8). When the second-row turbines experience both ridge- and turbine-induced turbulence, the disc-averaged turbulence intensity increases while onset flow velocity decreases (Figure 9), leading to a decrease in DEL (Table 2).

Table 2. Damage Equivalent Loads (DEL) of blade thrust for second-row turbines, along with cases 2D and 6D representing second-row turbines operating in absence of the first-row turbines. Data normalised to the value for the first row (and isolated) turbine on a flat-bed, DEL_0 .

Case	F8	F12	6U8	6U12	2U8	2D	6D
DEL/DEL_0	0.942	0.972	1.430	1.232	1.054	1.792	1.583

To better understand the contribution of onset flow velocity, vertical shear, and turbulence to fatigue loads, the power spectral density (PSD) with frequencies normalised by the blade passing frequency ($f_0 = \Omega/2\pi$) and probability of exceedance (PoE) of the rotor thrust force are analysed (Figure 10). In the PSD plot, shaded areas represent the range of spectra from the first- (red) and second-row turbines (grey), while solid lines depict cases 2D and 6D, i.e., with only the second-row turbines operating downstream of the ridge without the first-row turbines. The spectra of all cases exhibit dominant frequency peaks at the blade passing frequency f_0 and its harmonics. Over the lower frequency range, i.e., $f/f_0 \leq 1$, turbines are subjected to the open-channel coherent structures at a normalised frequency of about 0.07 equivalent to a Strouhal number $St = f \cdot L_x/U_0 = 0.29$, where L_x is the inflow streamwise length scale. The spectral energy is largest at this frequency for all cases, with the peak value at the second-row turbines being greater than at the first-row turbines due to the turbulent wakes from the ridge and upstream turbine. Over the frequency range $f/f_0 \geq 0.1$, the spectral energy content for the second-row turbines (grey shaded region in Figure 10a) is larger than for upstream turbines, mainly due to the increased turbulence from the first-row turbine wakes (Figure 9b). In the absence of the first-row turbines, the PSD of the 2D case over the lower frequency range ($f/f_0 \leq 1$) shows a reduction in spectral energy content compared to that of second-row turbines, while at $f/f_0 \approx 0.06$, the peak spectral energy is the highest due to the influence of the ridge-induced turbulence. The PSD of the 6D case falls within the range of the second-row turbines despite having a lower disc-averaged turbulence intensity than the 2D case (Figure 9b). This difference in the PSD between 2D and 6D indicates that the ridge-induced turbulence at the 6D location is more isotropic over the rotor area compared to the 2D location, in which the large-scale structures of the ridge dominate, especially at low frequencies (Figure 8). The higher PSD peaks are associated with an increased flow shear, whereby inducing larger blade load variations occur when they sweep over the top and bottom ends of the rotor swept area, as shown in the variation in maximum and minimum velocity values (Figure 9a).

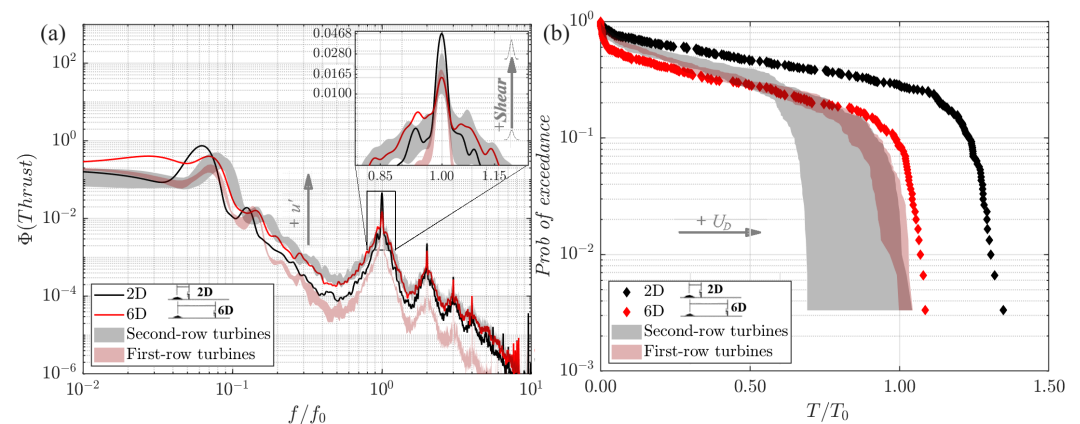


Figure 10. (a) Power spectral density (PSD) of rotor thrust load with frequency normalised by the blade passing frequency f_0 and (b) probability of exceedance (PoE) for the rotor thrust load normalised by the maximum load of the flat-bed case (T_0).

The largest fatigue loads occur from a combination of flow variables, such as high disc-averaged velocity, spatially varying velocity, and turbulence intensity. Larger disc-averaged velocities (Figure 9a) lead to increasing maximum rotor thrust values (accounted for as probability of exceedance of loads, Figure 10b). For instance, for the 2D case, the probability of exceeding a high load is largest (Figure 10b), as this position has the highest disc-averaged velocity (Figure 9). However, there is no correlation of the velocity with DEL values (Table 2). Considering the 2U8 case, the increase in onset turbulence due to the wake of the first-row turbine accompanies a decrease in onset velocity and shear, together with a more heterogeneous turbulence distribution over the swept area (compare the 2D and 2U8 cases in Figures 8 and 9). Consequently, DEL for 6U8 reduces by about 20% compared to the 2D case. Additionally, the PoE for first-row turbines shows a higher probability of high load occurrence (high disc-averaged velocity) than for most of the second-row turbine locations (see Figures 9a and 10b). However, their damage equivalent load, DEL_0 , is lower than the DEL of the second-row turbines in the ridge cases (6U8, 6U12, and 2U8 in Table 2). This increase in the DEL value in the ridge cases compared to DEL_0 indicates that spatial variation of the onset turbulence is important to consider when evaluating DEL.

3.3. Assessment of Load Prediction with BEMT

This section discusses the accuracy of a predictive approach for second-row turbine loading based on the Blade Element Momentum Theory (BEMT) that is fed with LES-generated onset planes with the front turbine only. In some earlier works, a distance of two-diameter upstream of the turbine is used to analyse the rotor performance [49] in accordance with the industry standards [50]. Over a distance of two diameters, the reduction in disc averaged velocity can be considered small. However, for downstream turbines, disc-averaged velocity increases over the same distance due to wake recovery, along with changes to the spatial variation. This leads to uncertainty regarding the onset flow location to employ for accurate load prediction. Here, loads predicted with a BEMT are assessed using the onset planes extracted both at the downstream rotor location ($x/D = 0$) or one diameter upstream ($x/D = -1$) [32]. Disc-averaged velocity and turbulence intensity in the induction region of the turbine are shown in Figure 7, and a summary of the streamwise variation in disc-averaged velocities upstream of the turbines, for cases with and without the presence of the upstream turbine or ridge, is presented in Appendix B.

Using the blade loading time series from the LES-ALM and BEMT, covering a period of 60 s at a sampling frequency of 200 Hz, Figure 11 compares the predictions of the DEL for the second-row turbines. For the flat-bed cases, BEMT slightly underestimates the DEL compared with the LES-ALM by 9.6% in F8 and 2.7% in F12 when the onset planes are taken at the rotor position, whereas similar DEL is obtained when the onset planes are extracted one diameter upstream of the second turbine. In the configurations with the ridge and first-row turbine, BEMT overestimates the fatigue loads when using the onset planes at the rotor location ($x/D = 0$). The discrepancies between BEMT and LES-ALM are most pronounced in the 6U12 case, with a difference of 35%, which reduces to 13.5% in the 6U8 and 2U8 cases. At these locations, the ridge induces heterogeneous flow characteristics, impacting the velocity, shear, and turbulence properties across the rotor location for second-row turbines, with a relatively quick change in pressure and turbulence over a small streamwise distance (Figure 3). Comparing the two cases in which the second turbine is $6D$ downstream of the ridge (2U8 and 6U12) shows better agreement between BEMT and ALM for the 2U8 case. This is due to the upstream turbine proximity to the ridge, whose wake impacts the coherence of the ridge-induced turbulence (Figure 8), thus leading to a more uniform distribution of turbulence in the onset flow to the downstream turbine [20].

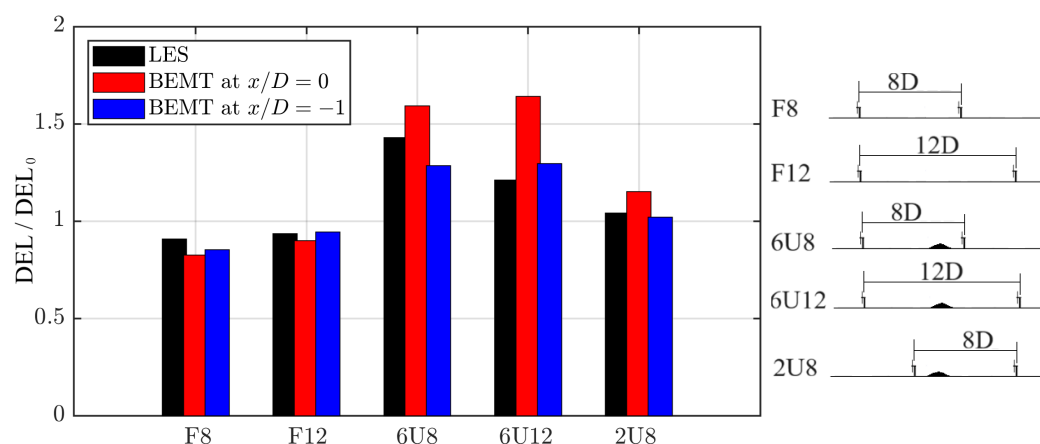


Figure 11. Normalised Damage Equivalent Loads (DEL/DEL_0) of blade thrust load in second-row turbines, obtained from LES–ALM (black) and BEMT calculated using inflow planes from the base-flow LES at the turbine position (red) and one diameter upstream (blue), normalised by the value of the first-row turbine in flat-bed conditions, $DEL_0 = 0.980$ N.

Adopting onset planes at one diameter upstream of the second turbine leads to a notable improvement in BEMT predictions, with deviations in DEL lowering to -10.07% , 7.10% , and -1.92% for cases 6U8, 6U12, and 2U8, respectively, in reference to LES–ALM. Due to the spatially varying flow conditions of the analysed cases (Figure 7), extracting the onset planes at the turbine location for BEMT does not represent the same inflow conditions that drive turbine loading in the LES–ALM. For instance, the induction generated by the turbine (implicitly captured in the LES–ALM), which disturbs the onset flow velocity and turbulence, is not fully accounted for in the BEMT. This has a minor effect when considering flat-bed cases, but becomes of increasing importance when relatively large pressure gradients [51] and/or coherent turbulent structures [52] appear. In the cases studied here, coherent structures are developed due to the wake of the upstream ridge; however, similar phenomena may be expected due to other bathymetric features or turbine wake interaction in arrays.

The spatial variability of the flow field is characterised by two-point correlation of the streamwise velocities relative to the rotor’s centre for the flat-bed case TF and the ridge cases 6U and 2U, at the second turbine position and one diameter upstream (Figure 12). Onset planes are also analysed one diameter upstream whilst the second turbine is operating (F8, 6U12 and 2U8) to account for the impact of the turbine’s induction in the onset turbulent flow field. For all cases, the region of positive spatial correlation is larger at the rotor position than at one diameter upstream. In the presence of the second-row turbine, the turbine’s induction impacts the approach flow coherence, reducing the region of positive correlation and resulting in larger negative correlation with the flow outside of the rotor region. This distribution is closer to the correlation obtained one diameter upstream than at the rotor position when the downstream turbine is not modelled. These two-point correlation contours highlight the spatial variability of the flow due to the wakes of the upstream turbine and ridge. In turn, cases with the seabed ridge (e.g., cases 6U12 and 2U8, Figure 12) experience a notable pressure gradient that restricts the direct applicability of the Taylor’s frozen turbulence hypothesis for the turbine’s induction region, as turbulent flow structures are not solely driven by the mean flow velocity. This is reflected in the DEL predictions (Figure 11), as there is an improved prediction from BEMT when adopting onset planes at which the flow spatial coherence resembles more closely that in the LES–ALM due to the turbine’s induction.

The PoE of the blade thrust load normalised by the value a first-row turbine in flat-bed conditions (T/T_0) for the ridge cases (6U8, 6U12, and 2U8) and F8 case are compared

between BEMT and LES–ALM over a load duration of 60 s and sampling frequency of 200 Hz (Figure 13). When the onset planes are taken at the rotor position, BEMT predicts slightly higher extreme loads, with an increase of 9.3% in 6U12, 7.9% in 6U8, and 2.7% in 2U8 compared to LES–ALM data, while for the F8 case, BEMT predicts a 2.3% lower extreme load than LES–ALM. The agreement for extreme loads improves when the inflow for BEMT is taken one diameter upstream, especially for 2U8 and 6U12. For the case 6U8, there is a notably larger shear induced by the ridge at the plane location $x/D = -1$ than at $x/D = 0$, which increases the steepness in the PoE distribution of thrust values for the probabilities below 10%.

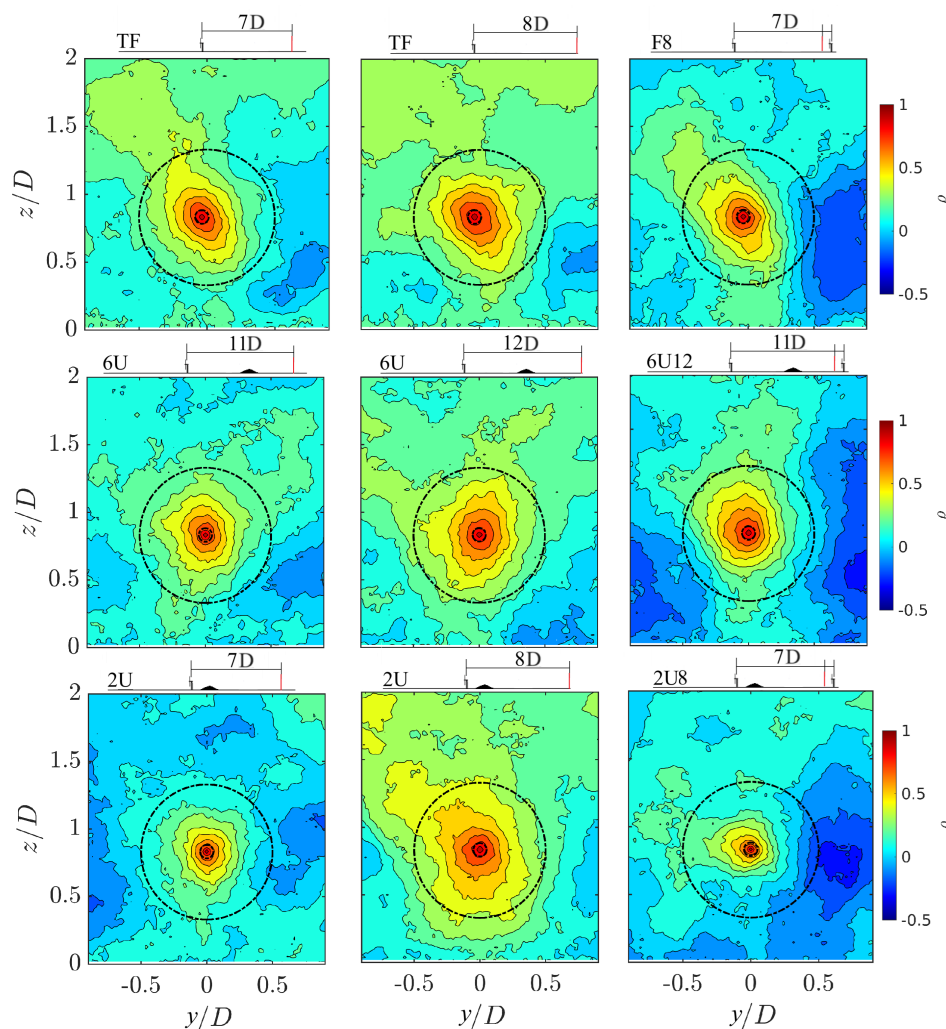


Figure 12. Contours of two-point correlation of the streamwise velocity ρ_{uu} in the yz -planes for cases TF and F8 (**top**), 6U and 6U12 (**middle**), and 2U and 2U8 (**bottom**). Dashed circles indicate the rotor swept area.

The PSD of the blade thrust force between the BEMT and LES–ALM is shown in Figure 14. While the BEMT predicts the overall trend, namely, the frequency of the onset large-scale turbulence ($f/f_0 \approx 0.8$) and the harmonics of the blade-passing ($f/f_0 \approx 0.33$), it overpredicts the spectral energy at these peaks compared to LES–ALM, especially when the data is taken at $x/D = 0$ in cases with the ridge (Figure 14a–c). This overestimation in spectral content implies there is more energy at those frequencies impinging onto the turbine from the onset flow in the BEMT than in the LES–ALM, which can be linked to the BEMT not accurately accounting for the influence of turbine induction on the onset flow (Figure 12). However, when the inflow for BEMT is taken at $x/D = -1$, the spectral

energy at peaks in the lower frequency range, specifically for $f/f_0 \geq 0.33$, is lower than the LES–ALM in the ridge cases (6U8, 6U12, and 2U8) due to the spatial variation in the ridge-induced structures (Figure 12). Additionally, the differences between the BEMT and LES–ALM in their spectral energy around the blade-passing frequency peak are consistent with the DEL values obtained from these methods (Figure 11).

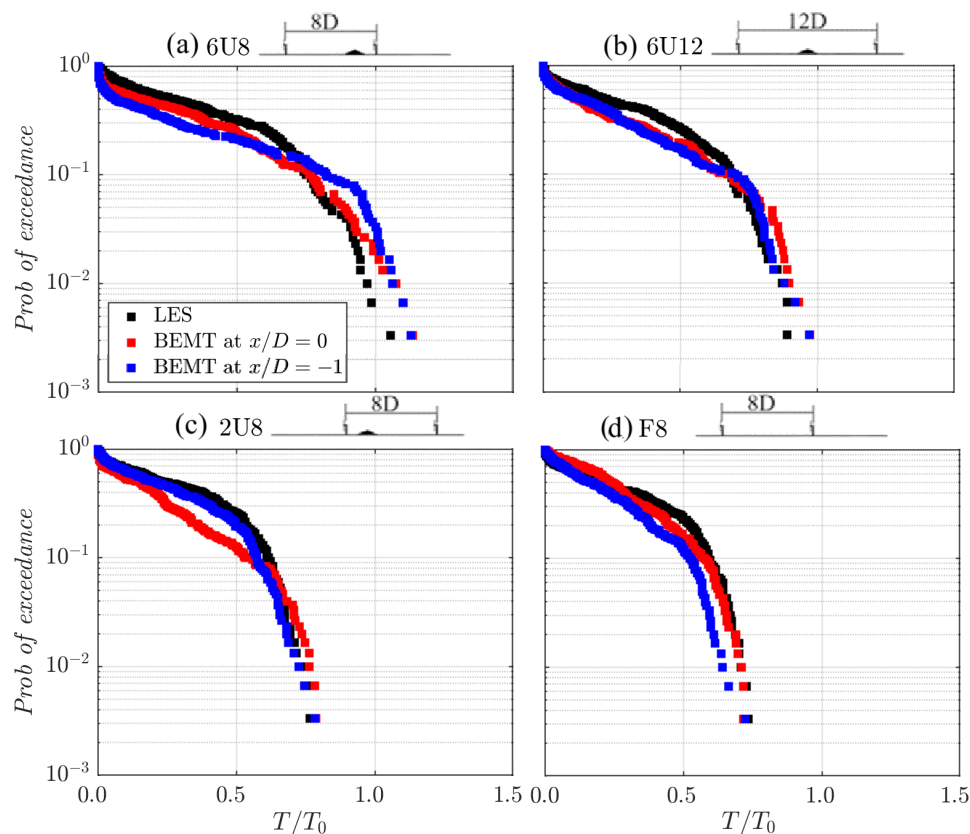


Figure 13. Probability of exceedance (PoE) of the blade thrust loads normalised by the maximum blade thrust obtained for flat-bed conditions (T/T_0) from the LES–ALM (black) and BEMT (red) for cases (a) 6U8, (b) 6U12, (c) 2U8, and (d) F8.

To further understand the effect of turbine presence on the onset conditions, the PSD of the streamwise and spanwise velocity signals are computed at hub-height and $-1D$ upstream of the second-row location for cases 6U12 and 2U8, in which the second-row turbine is located at $6D$ downstream of the ridge. For completeness, PSD in three simulation scenarios are compared: only with the first-row turbine, with both first and second rows, and with the ridge only (Figure 15). Frequency peaks over the low-frequency range, $f/f_0 \leq 0.1$, appear in all three scenarios (Figures 15a,b), which are consistent with those peaks observed in the PSD of the rotor and blade thrust load (Figures 10a and 14). In the PSD of ridge only (labelled as “2RD”), there is higher spectral energy compared to the 6U12 and 2U8 cases for both u and v velocities, suggesting large-scale turbulent structures are more energetic for this case without turbines at this location (Figure 15). It can be seen that spectral energy at the ridge-induced shedding frequency, $f/f_0 \approx 0.04$ (blue line in Figure 15c,d), is impacted by the first-row turbine, which attenuates the energetic turbulent structures induced by the ridge.

Considering the wake meandering frequency of the first-row turbine, a peak in the PSD of v velocities suggests this is at $f/f_0 \approx 0.053$ for the case 6U12, while at $f/f_0 \approx 0.067$ in the 2U8 case. Nevertheless, no peaks are observed in the PSD of the thrust loads (Figure 14) that are linked to the wake meandering of the first-row turbine, and thus this does not have a significant impact on the load on the second-row turbine, as the first-turbine’s wake mixes rapidly due to the ridge influence.

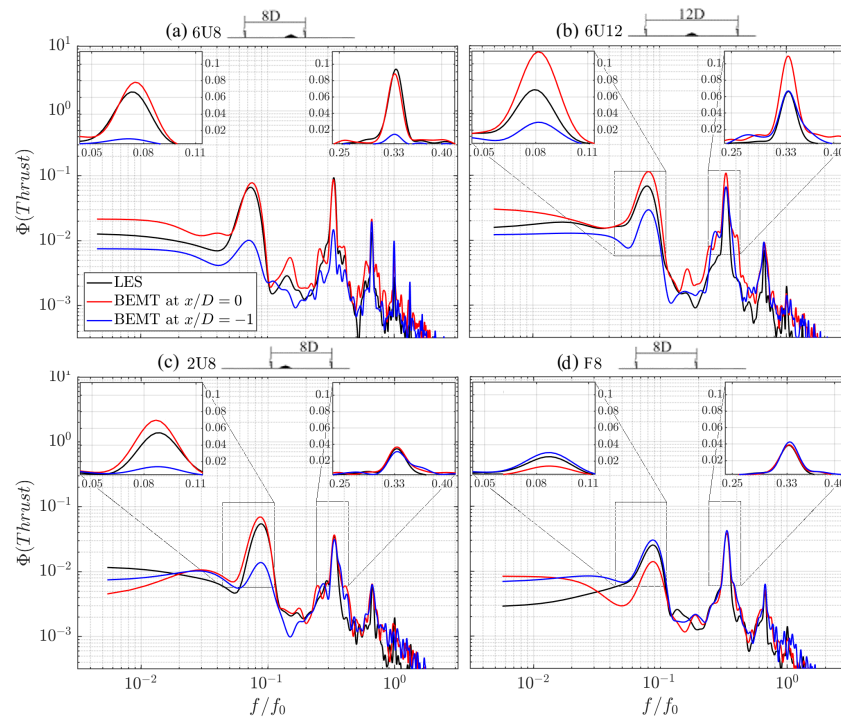


Figure 14. Power spectral density (PSD) of the blade thrust load from the LES–ALM (black) and BEMT (red) for cases (a) 6U8, (b) 6U12, (c) 2U8, and (d) F8. The frequency is normalised by the blade passing frequency f_0 .

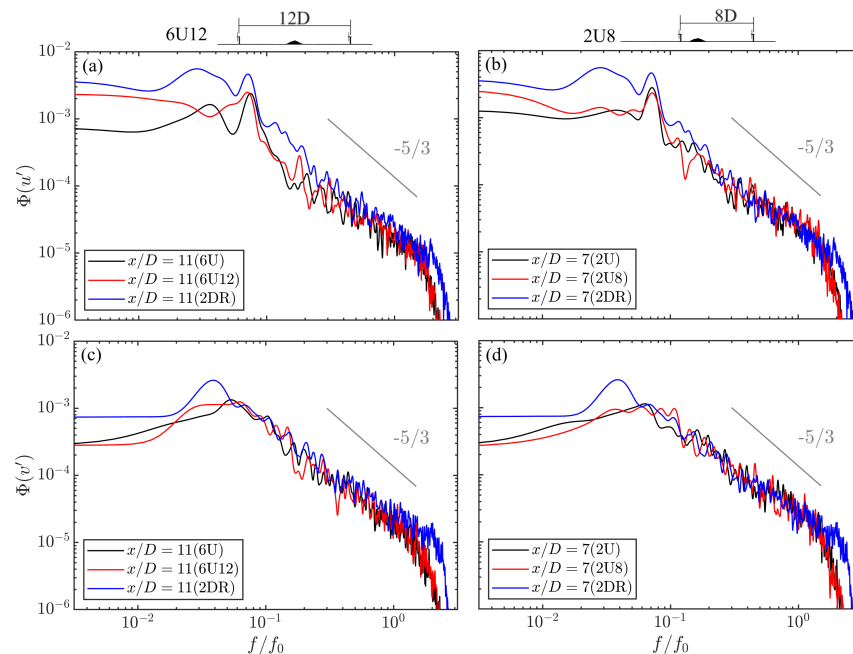


Figure 15. Comparison of the power spectral density (PSD) profiles of the streamwise (a,b) and spanwise (c,d) velocity time series obtained from LES at one diameter upstream of the second-row turbine location, with and without its presence compared to the ridge only case (2DR). (a,c) 6U12 and 6U cases. (b,d) 2U8 and 2U cases. The frequency is normalised by the blade passing frequency f_0 and the location x/D of the sampling points is relative to the first-row turbine.

4. Conclusions

Large-eddy simulations (LES) have been conducted to study the wake of a tidal turbine interacting with a seabed ridge and the resultant loading of a downstream turbine. The rate of recovery of the tidal turbine wake is found to be enhanced by interaction

with the ridge, due to the pressure gradient developed. Whilst streamwise recovery is enhanced, the lateral profile of the wake is well described by a self-similar Gaussian profile to distances of 12 diameters (D) downstream. When a second turbine is located within the wake, an induction region is observed, and disc averaged velocity in this region is well captured by vortex sheet theory superposed with the recovering wake velocity. The presence of the second turbine is also found to modify the coherent structures that otherwise develop downstream of the ridge. This results in turbine blade fatigue loads that are larger than due to the upstream turbine only, but less than due to the upstream ridge only.

Prediction of turbine loading using BEMT was assessed using time-varying inflow planes extracted from LES without the downstream turbine included in the simulation. Use of the onset flow extracted at one diameter upstream from the turbine location is found to provide predictions of Damage Equivalent Loads (DEL) to within 10% of LES with an actuator-line method (LES-ALM). At this upstream distance, the spatial variation of onset velocity and of turbulence is similar to the onset flow to the downstream turbine when simulated in the LES. Notably, this differs from the recommendation of two diameters upstream given in tidal stream turbine design standards. Power spectral density analysis of blade thrust loading showed that cases with largest fatigue load variation were those in which the BEMT predicted larger spectral energy at the blade passing frequency. Discrepancy between BEMT and LES-ALM was largest for locations $2D$ downstream of the ridge, and this is attributed to the pressure gradient generated by the ridge and role of the coherent turbulent structures shed by this ridge shape, both of which restrict the application of Taylor's frozen turbulence hypothesis, which is widely applied in BEMT load models.

These findings have implications for the micro-siting of turbine arrays within the varying bathymetry of tidal stream sites, highlighting that pressure gradients can alter wake recovery and turbulence and hence affect downstream rotor performance and loading. Such loads can be reasonably predicted at low compute cost with BEMT, which also offers scope to explore load mitigation techniques, but such predictions rely on careful definition of onset conditions. This demands the use of high-fidelity flow models to adequately account for pressure gradients and their impact on wakes and turbulence characteristics, and to investigate turbine wakes in arrays located within irregular bathymetry.

Author Contributions: Conceptualisation, S.H., P.O. and T.S.; methodology, S.H., H.M., P.O. and T.S.; software, S.H., H.M. and P.O.; validation, S.H., H.M. and P.O.; formal analysis, S.H., H.M., P.O. and T.S.; investigation, S.H. and H.M.; resources, S.H. and P.O.; data curation, S.H. and H.M.; writing—original draft preparation, S.H., H.M. and P.O.; writing—review and editing, S.H., H.M., P.O., P.S. and T.S.; visualization, S.H.; supervision, P.O., P.S. and T.S.; funding acquisition, P.O. and T.S. All authors have read and agreed to the published version of the manuscript.

Funding: This work was supported by a PhD studentship awarded by Jazan University, Saudi Arabia, and partly funded by EPSRC (Engineering and Physical Sciences Research Council) Supergen Offshore Renewable Energy Impact Hub (grant no. EP/Y016297/1).

Data Availability Statement: Data supporting the conclusions of the study are provided in the 'Results' section and Appendices A and B of this paper. Further raw data will be made available by the authors on request.

Acknowledgments: Access to the ARCHER2 UK National Supercomputing Service (<https://www.archer2.ac.uk>, accessed on 1 December 2024), partly provided by the UK Turbulence Consortium (UKTC) under EPSRC grant no. EP/R029326/1, and the UK High-End Computing Consortium for Wave Structure Interaction (HEC-WSI) (<http://hec-wsi.ac.uk>, accessed on 1 December 2024), supported by EPSRC (grant no. EP/X035751/1), is also acknowledged.

Conflicts of Interest: The authors declare that they have no known competing financial interests or personal relationships that could have appeared to influence the work reported in this paper.

Abbreviations

The following abbreviations are used in this manuscript:

ALM	Actuator Line Model
APG	Adverse Pressure Gradient
BEMT	Blade Element Momentum Theory
CPU	Central Processing Unit
DEL	Damage Equivalent Load
DOFAS	Digital Offshore Farm Simulator
FPG	Favourable Pressure Gradient
HPC	High-Performance Computing
IBM	Immersed Boundary Method
LES	Large-Eddy Simulation
MPI	Message Passing Interface
PoE	Probability of Exceedance
PSD	Power Spectral Density
TI	Turbulence Intensity
TSR	Tip Speed Ratio
WALE	Wall-Adapting Local-Eddy

Appendix A. Shear at Turbine Location

Figure A1 shows the normalised turbulent momentum shear stress ($-u'w'/U_0^2$) at the turbine locations. When only the ridge is located upstream of the turbines, e.g., the 2D and 6D cases, a negative vertical turbulent flux results from the downward movement of the fluxes from the accelerated flow above the ridge towards the slower flow in the ridge wake. However, the presence of a first-row turbine upstream of the ridge, as in the 6U8 case, reduces the vertical extent of the shear layer. This reduction suggests that when the low-momentum turbine wake merges with the low-momentum flow in the ridge wake, there is a notable reduction in vertical momentum transport. For the 6U12 and 2U8 cases, the distribution of $-u'w'$ over the rotor area is more evenly distributed compared to the 6D case, where no upstream turbine is present. Considering the flat-bed configurations, the $-u'w'$ distribution in the F8 case shows greater downwards movement from the bypass flow toward the top half of the turbine wake region than in the F12 case. This pattern of momentum transport into the wake is consistent across all 8D spacing cases, regardless of ridge presence.

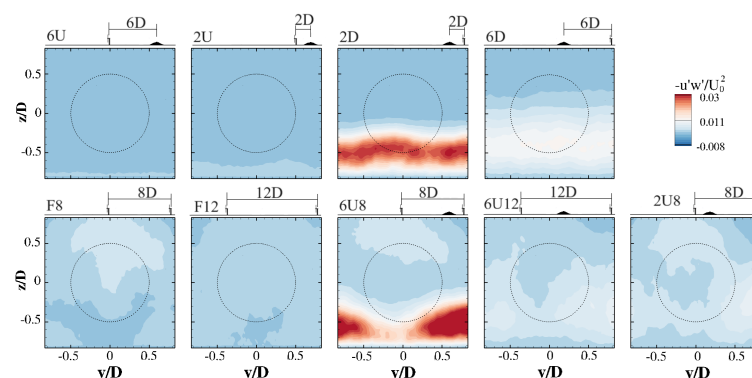


Figure A1. Reynolds shear stress contours in the yz -plane from the base-flow simulations at turbine locations, dashed circles indicates the rotor area. The top row shows cases with no upstream turbine, and the bottom row depicts scenarios where an upstream turbine is present.

Appendix B. Reference Velocity

Table A1 presents a comparison of the disc-averaged velocity upstream of the second-row turbines. Initially, the upstream distance at which the induction from the second-row turbines is approximately similar to the base-flow varies based on the case condition, i.e., a wide range is found with the values larger than $2D$ in F8 case and less than $1D$ in 6U8 case. The upstream distance $2D$ is commonly used in the literature (e.g., see Refs. [25,32]). However, in second-row turbines, the velocity at this upstream distance might not represent the turbine onset velocity due to the wake effect of first-row turbines, as seen in case F8 in Table A1. In contrast, in case of the ridge presence, a $2D$ distance upstream of the second-row turbine is sufficient to analyse the onset conditions on second-row turbines when the turbine is far from the ridge due to the non-uniform pressure induced by the ridge, as seen in case 6U8.

Table A1. Comparison of the disc-averaged velocity (U_D) upstream of the second-row turbines. The second column from left shows (U_{DT}) the disc-averaged velocity at the merge distance (last column, in diameters D) where the induction from the second-row turbines is approximately vanished. The third and fourth columns shows U_D at $1D$ and $2D$ upstream of the second-row turbines.

Case	U_{DT} [m s ⁻¹]	U_D/U_{DT} ($x/D = -1$) [-]	U_D/U_{DT} ($x/D = -2$) [-]	Merge Distance [D]
F8	0.375	0.917	0.904	2.185
F12	0.405	0.938	0.949	1.722
6U8	0.466	1.032	0.994	0.944
6U12	0.432	0.949	0.979	1.833
2U8	0.392	0.944	0.969	1.722
Second-row only (no upstream turbine)				
TF	0.476	0.947	0.973	1.889
2D	0.543	1.028	1.029	0.611
6D	0.483	0.954	0.994	3.556

References

1. Coles, D.; Angeloudis, A.; Greaves, D.; Hastie, G.; Lewis, M.; Mackie, L.; McNaughton, J.; Miles, J.; Neill, S.; Piggott, M.; et al. A review of the UK and British Channel Islands practical tidal stream energy resource. *Proc. R. Soc. A* **2021**, *477*, 20210469. [[CrossRef](#)] [[PubMed](#)]
2. Guillou, N.; Neill, S.P.; Robins, P.E. Characterising the tidal stream power resource around France using a high-resolution harmonic database. *Renew. Energy* **2018**, *123*, 706–718. [[CrossRef](#)]
3. Stokesbury, M.J.; Logan-Chesney, L.M.; McLean, M.F.; Buhariwalla, C.F.; Redden, A.M.; Beardsall, J.W.; Broome, J.E.; Dadswell, M.J. Atlantic sturgeon spatial and temporal distribution in Minas Passage, Nova Scotia, Canada, a region of future tidal energy extraction. *PLoS ONE* **2016**, *11*, e0158387. [[CrossRef](#)]
4. Novo, P.G.; Kyozuka, Y. Tidal stream energy as a potential continuous power producer: A case study for West Japan. *Energy Convers. Manag.* **2021**, *245*, 114533. [[CrossRef](#)]
5. Marsh, P.; Penesis, I.; Nader, J.R.; Cossu, R. Multi-criteria evaluation of potential Australian tidal energy sites. *Renew. Energy* **2021**, *175*, 453–469. [[CrossRef](#)]
6. Abundo, M.L.; Nerves, A.C.; Ang, M.R.C.; Paringit, E.C.; Bernardo, L.P.; Villanoy, C.L. Energy potential metric for rapid macro-level resource assessment of tidal in-stream energy in the Philippines. In Proceedings of the 2011 10th International Conference on Environment and Electrical Engineering, Rome, Italy, 8–11 May 2011; IEEE: Piscataway, NJ, USA, 2011; pp. 1–4. [[CrossRef](#)]
7. Jiang, C.; Kang, Y.; Qu, K.; Kraatz, S.; Deng, B.; Zhao, E.; Wu, Z.; Chen, J. High-resolution numerical survey of potential sites for tidal energy extraction along coastline of China under sea-level-rise condition. *Ocean Eng.* **2021**, *236*, 109492. [[CrossRef](#)]
8. Huchet, M.; Droniou, E.; Perez, L.; Vermeulen, B.; Baldock, A.; Johnson, F.; Boake, C. Wake characterization of tidal turbines in the Pentland Firth using vessel-mounted ADCP measurements. In Proceedings of the 15th European Wave and Tidal Energy Conference, Bilbao, Spain, 3–7 September 2023; Volume 15. [[CrossRef](#)]

9. Ouro, P.; Stansby, P.; Macleod, A.; Stallard, T.; Mullings, H. High-fidelity modelling of a six-turbine tidal array in the Shetlands. In Proceedings of the 15th European Wave and Tidal Energy Conference, Bilbao, Spain, 3–7 September 2023; Volume 15. [\[CrossRef\]](#)
10. Jordan, C.; Dundovic, D.; Fragkou, A.K.; Deskos, G.; Coles, D.S.; Piggott, M.D.; Angeloudis, A. Combining shallow-water and analytical wake models for tidal array micro-siting. *J. Ocean Eng. Mar. Energy* **2022**, *8*, 193–215. [\[CrossRef\]](#)
11. Adcock, T.A.; Draper, S.; Willden, R.H.; Vogel, C.R. The fluid mechanics of tidal stream energy conversion. *Annu. Rev. Fluid Mech.* **2021**, *53*, 287–310. [\[CrossRef\]](#)
12. Liu, L.; Stevens, R.J. Effects of two-dimensional steep hills on the performance of wind turbines and wind farms. *Bound.-Layer Meteorol.* **2020**, *176*, 251–269. [\[CrossRef\]](#)
13. Cai, T.; Cheng, S.; Segalini, A.; Chamorro, L.P. Local topography-induced pressure gradient effects on the wake and power output of a model wind turbine. *Theor. Appl. Mech. Lett.* **2021**, *11*, 100297. [\[CrossRef\]](#)
14. Tian, W.; Zheng, K.; Hu, H. Investigation of the wake propagation behind wind turbines over hilly terrain with different slope gradients. *J. Wind Eng. Ind. Aerodyn.* **2021**, *215*, 104683. [\[CrossRef\]](#)
15. Zhang, Z.; Huang, P.; Bitsuamlak, G.; Cao, S. Large-eddy simulation of wind-turbine wakes over two-dimensional hills. *Phys. Fluids* **2022**, *34*, 065123. [\[CrossRef\]](#)
16. Siguenza-Alvarado, D.; Pulletikurthi, V.; Quinones, J.J.; Nelson, C.; Cheng, S.; Doosttalab, A.; Chamorro, L.P.; Castillo, L. Wake interaction of aligned wind turbines over two-dimensional hills. *Phys. Fluids* **2023**, *35*, 105142. [\[CrossRef\]](#)
17. Dar, A.S.; Gertler, A.S.; Porté-Agel, F. An experimental and analytical study of wind turbine wakes under pressure gradient. *Phys. Fluids* **2023**, *35*, 045140. [\[CrossRef\]](#)
18. Shamsoddin, S.; Porté-Agel, F. Wind turbine wakes over hills. *J. Fluid Mech.* **2018**, *855*, 671–702. [\[CrossRef\]](#)
19. Hurubi, S.; Stallard, T.; Stansby, P.; Mullings, H.; Ouro, P. Characterisation of turbulent flow and the wake of a tidal stream turbine in proximity to a ridge. In Proceedings of the 15th European Wave and Tidal Energy Conference, Bilbao, Spain, 3–7 September 2023; Volume 15. [\[CrossRef\]](#)
20. Hurubi, S.; Stallard, T.; Mullings, H.; Stansby, P.; Ouro, P. Numerical study of the effect of a ridge on the wake and loading of a tidal stream turbine. *J. Fluids Struct.* **2024**, *129*, 104158. [\[CrossRef\]](#)
21. Hyvärinen, A.; Segalini, A. Effects from complex terrain on wind-turbine performance. *J. Energy Resour. Technol.* **2017**, *139*, 051205. [\[CrossRef\]](#)
22. Dar, A.S.; Porté-Agel, F. Wind turbine wake superposition under pressure gradient. *Phys. Fluids* **2024**, *36*. [\[CrossRef\]](#)
23. McCann, G. Tidal current turbine fatigue loading sensitivity to waves and turbulence—a parametric study. In Proceedings of the 7th European Wave and Tidal Energy Conference, Porto, Portugal, 11–14 September 2007.
24. Mullings, H.; Stallard, T. Assessment of dependency of unsteady onset flow and resultant tidal turbine fatigue loads on measurement position at a tidal site. *Energies* **2021**, *14*, 5470. [\[CrossRef\]](#)
25. Gaurier, B.; Ikhennicheu, M.; Germain, G.; Druault, P. Experimental study of bathymetry generated turbulence on tidal turbine behaviour. *Renew. Energy* **2020**, *156*, 1158–1170. [\[CrossRef\]](#)
26. Ouro, P.; Stoesser, T. Impact of environmental turbulence on the performance and loadings of a tidal stream turbine. *Flow Turbul. Combust.* **2019**, *102*, 613–639. [\[CrossRef\]](#)
27. Mullings, H.; Draycott, S.; Thiébot, J.; Guillou, S.; Mercier, P.; Hardwick, J.; Mackay, E.; Thies, P.; Stallard, T. Evaluation of Model Predictions of the Unsteady Tidal Stream Resource and Turbine Fatigue Loads Relative to Multi-Point Flow Measurements at Raz Blanchard. *Energies* **2023**, *16*, 7057. [\[CrossRef\]](#)
28. Ouro, P.; Ramírez, L.; Harrold, M. Analysis of array spacing on tidal stream turbine farm performance using Large-Eddy Simulation. *J. Fluids Struct.* **2019**, *91*, 102732. [\[CrossRef\]](#)
29. Ouro, P.; Mullings, H.; Christou, A.; Draycott, S.; Stallard, T. Wake characteristics behind a tidal turbine with surface waves in turbulent flow analyzed with large-eddy simulation. *Phys. Rev. Fluids* **2024**, *9*, 034608. [\[CrossRef\]](#)
30. Mullings, H.; Stallard, T. Unsteady loading in a tidal array due to simulated turbulent onset flow. In Proceedings of the Advances in Renewable Energies Offshore: Proceedings of the 3rd International Conference on Renewable Energies Offshore (RENEW 2018), Lisbon, Portugal, 8–10 October 2018; CRC Press: Boca Raton, FL, USA, 2018; p. 227.
31. Mullings, H.; Stallard, T. Analysis of tidal turbine blade loading due to blade scale flow. *J. Fluids Struct.* **2022**, *114*, 103698. [\[CrossRef\]](#)
32. Mullings, H.; Amos, L.; Miller, C.; Ouro, P.; Stallard, T. Efficient prediction of tidal turbine fatigue loading using turbulent onset flow from Large Eddy Simulations. *J. Ocean. Eng. Mar. Energy* **2024**, *10*, 537–554. [\[CrossRef\]](#)
33. Ouro, P.; Lopez-Novoa, U.; Guest, M.F. On the performance of a highly-scalable Computational Fluid Dynamics code on AMD, ARM and Intel processor-based HPC systems. *Comput. Phys. Commun.* **2021**, *269*, 108105. [\[CrossRef\]](#)
34. Cevheri, M.; McSherry, R.; Stoesser, T. A local mesh refinement approach for large-eddy simulations of turbulent flows. *Int. J. Numer. Methods Fluids* **2016**, *82*, 261–285. [\[CrossRef\]](#)
35. Nicoud, F.; Ducros, F. Subgrid-scale stress modelling based on the square of the velocity gradient tensor. *Flow Turbul. Combust.* **1999**, *62*, 183–200. [\[CrossRef\]](#)

36. Ouro, P.; Harrold, M.; Ramirez, L.; Stoesser, T. Prediction of the Wake Behind a Horizontal Axis Tidal Turbine Using a LES-ALM. In *Recent Advances in CFD for Wind and Tidal Offshore Turbines*; Ferrer, E., Montlaur, A., Eds.; Springer: Berlin/Heidelberg, Germany, 2019; pp. 25–35. [[CrossRef](#)]
37. Churchfield, M.J.; Schreck, S.J.; Martinez, L.A.; Meneveau, C.; Spalart, P.R. An advanced actuator line method for wind energy applications and beyond. In *Proceedings of the 35th Wind Energy Symposium*, Grapevine, TX, USA, 9–13 January 2017; p. 1998. [[CrossRef](#)]
38. Shen, W.Z.; Sørensen, J.N.; Mikkelsen, R. Tip loss correction for actuator/Navier–Stokes computations. *J. Sol. Energy Eng.* **2005**, *127*, 209–213. [[CrossRef](#)]
39. Uhlmann, M. An immersed boundary method with direct forcing for the simulation of particulate flows. *J. Comput. Phys.* **2005**, *209*, 448–476. [[CrossRef](#)]
40. Stallard, T.; Feng, T.; Stansby, P. Experimental study of the mean wake of a tidal stream rotor in a shallow turbulent flow. *J. Fluids Struct.* **2015**, *54*, 235–246. [[CrossRef](#)]
41. Jarrin, N.; Prosser, R.; Uribe, J.C.; Benhamadouche, S.; Laurence, D. Reconstruction of turbulent fluctuations for hybrid RANS/LES simulations using a synthetic-eddy method. *Int. J. Heat Fluid Flow* **2009**, *30*, 435–442. [[CrossRef](#)]
42. Parkinson, S.G.; Collier, W.J. Model validation of hydrodynamic loads and performance of a full-scale tidal turbine using Tidal Bladed. *Int. J. Mar. Energy* **2016**, *16*, 279–297. [[CrossRef](#)]
43. *ASTM E1049-85(2017)*; Standard Practices for Cycle Counting in Fatigue Analysis. ASTM International: West Conshohocken, PA, USA, 2017.
44. Chanprasert, W.; Sharma, R.; Cater, J.; Norris, S. Large Eddy Simulation of wind turbine fatigue loading and yaw dynamics induced by wake turbulence. *Renew. Energy* **2022**, *190*, 208–222. [[CrossRef](#)]
45. de N Santos, F.; D’Antuono, P.; Robbelein, K.; Noppe, N.; Weijtjens, W.; Devriendt, C. Long-term fatigue estimation on offshore wind turbines interface loads through loss function physics-guided learning of neural networks. *Renew. Energy* **2023**, *205*, 461–474. [[CrossRef](#)]
46. Medici, D.; Ivanell, S.; Dahlberg, J.Å.; Alfredsson, P.H. The upstream flow of a wind turbine: Blockage effect. *Wind Energy* **2011**, *14*, 691–697. [[CrossRef](#)]
47. Harrold, M.; Ouro, P. Rotor loading characteristics of a full-scale tidal turbine. *Energies* **2019**, *12*, 1035. [[CrossRef](#)]
48. Bastankhah, M.; Porté-Agel, F. Wind tunnel study of the wind turbine interaction with a boundary-layer flow: Upwind region, turbine performance, and wake region. *Phys. Fluids* **2017**, *29*, 065105. [[CrossRef](#)]
49. Evans, L.; Ashton, I.; Sellar, B. Tidal turbine power performance assessments following IEC TS 62600-200 using measured and modelled power outputs. *Renew. Energy* **2023**, *212*, 138–150. [[CrossRef](#)]
50. *PD IEC/TS 62600-200:2013*; Marine Energy. Wave, Tidal and Other Water Current Converters: Electricity Producing Tidal Energy Converters. Power Performance Assessment. International Electrotechnical Commission (IEC): Geneva, Switzerland, 2013.
51. Graham, J.M.R. Rapid distortion of turbulence into an open turbine rotor. *J. Fluid Mech.* **2017**, *825*, 764–794. [[CrossRef](#)]
52. Deskos, G.; Payne, G.S.; Gaurier, B.; Graham, M. On the spectral behaviour of the turbulence-driven power fluctuations of horizontal-axis turbines. *J. Fluid Mech.* **2020**, *904*, A13. [[CrossRef](#)]

Disclaimer/Publisher’s Note: The statements, opinions and data contained in all publications are solely those of the individual author(s) and contributor(s) and not of MDPI and/or the editor(s). MDPI and/or the editor(s) disclaim responsibility for any injury to people or property resulting from any ideas, methods, instructions or products referred to in the content.